Uniaxial pressure effects, phase diagram, and tricritical point in the centrosymmetric skyrmion lattice magnet $GdRu_2Si_2$

L. Gries,[1] T. Kleinbeck,[1] D. A. Mayoh,[2] G. D. A. Wood,[2] G. Balakrishnan,[2] and R. Klingeler[1,*]

[1]*Kirchhoff Institute of Physics, Heidelberg University, INF 227, D-69120 Heidelberg, Germany*

[2]*Department of Physics, University of Warwick, Coventry, West Midlands CV4 7AL, United Kingdom*

(Received 5 November 2024; accepted 5 February 2025; published 18 February 2025)

The magnetic phase diagram, magnetoelastic coupling, and uniaxial pressure effects of centrosymmetric magnetic skyrmion-hosting $GdRu_2Si_2$ are investigated by means of high-resolution capacitance dilatometry in fields up to 15 T supported by specific-heat and magnetization studies. In addition to the previously reported phases in the H-T phase diagram, we observe a third antiferromagnetic phase in zero magnetic field. We present the magnetic phase diagram and find two unreported phases, one of which features a comparably giant uniaxial pressure dependence. Our dilatometric measurements show magnetoelastic effects associated with the various magnetic ordering phenomena. We determine the uniaxial pressure dependencies of the various phases, in particular of the skyrmion lattice phase which is enhanced at higher fields and temperatures and also widens at a rate of 0.07 T/GPa when uniaxial pressure is applied along the c axis. The relevance of fluctuations is further highlighted by the presence of a tricritical point indicated by our thermodynamic data at the phase boundary separating two double-Q magnetic configurations between which the skyrmion pocket phase evolves upon further cooling.

DOI: 10.1103/PhysRevB.111.064419

I. INTRODUCTION

Magnetic skyrmions are a class of topologically protected noncollinear spin structures which exhibit a variety of particlelike properties [1–6]. The nanometric scale of magnetic skyrmions and emergence of interesting phenomena such as the topological Hall effect [7–9] and nonlinear tunneling magnetoresistance [10] lead to the proposition of novel skyrmion-based technological applications including neuromorphic computation systems [11–13], nonvolatile memory [14–16], and logical gates [17–19]. Since the initial experimental finding of magnetic skyrmions in MnSi in 2009 by Mühlbauer *et al.* [20], a plethora of systems hosting a skyrmion lattice have been discovered, e.g., Cu_2OSeO_3 [21], GaV_4S_8 [22], and thin-film $Fe_{0.5}Co_{0.5}Si$ [23]. In these noncentrosymmetric systems, the Dzyaloshinskii-Moriya interaction is an integral part of the skyrmion formation process. However, this is not the case in selected centrosymmetric systems such as Gd_2PdSi_3 [24], $Gd_3Ru_4Al_{12}$ [25], $EuAl_4$ [26], and $GdRu_2Si_2$ [27,28], where various stabilization mechanisms from geometric frustration [29,30] to multiple spin interactions [31] have been proposed. These centrosymmetric systems are interesting for the aforementioned technological applications due to their small skyrmion diameter of the order of ∼2 nm [14,25,28].

$GdRu_2Si_2$ crystallizes in centrosymmetric tetragonal structure in the space group $I4/mmm$ [32–34]. It consists of square layers of Gd^{3+} ions ($S = 7/2, L = 0$) and Ru_2Si_2 layers alternatingly stacked along the c axis. In zero magnetic field, two distinct magnetic phases have been reported: phase IV (magnetic phases are labeled in accordance with [35]) which evolves at $T_N \simeq 46$ K and phase I which evolves below $T_t \simeq 40$ K [27,36]. Neutron diffraction experiments reveal that phase IV assumes a sinusoidal or helical spin structure [37], while phase I, the ground state, forms a double-Q constant moment structure [35]. Applying magnetic fields parallel to the c axis induces a first-order phase transition at about 2 T below 20 K [36]. It features a double-Q magnetic structure consisting of the superposition of two orthogonal helices creating a skyrmion lattice (SKL) in this field-induced phase II [27,28]. By further increasing $B||c$, the SKL phase is replaced by a double-Q magnetic structure in phase III above 2.4 T, while full polarization of the spin structure is achieved for $B||c \gtrsim 10$ T [27]. The origin of the observed magnetic structures has been mainly attributed to a combination of Ruderman-Kittel-Kasuya-Yosida (RKKY) and multiple spin interactions [28,38–40].

Here we report magnetoelastic coupling and the initial uniaxial pressure dependencies on the various phases in $GdRu_2Si_2$, as well as the discovery of two magnetic phases, VI and VII. We achieve this by means of high-resolution capacitance dilatometry studies to determine thermal expansion and magnetostriction in fields up to $B||c = 14$ T, which are supported by magnetization and specific-heat measurements. In addition to further completing the magnetic phase diagram, we report the thermodynamic properties at the phase boundaries, including evidence of a tricritical point and widening of the SKL phase upon application of uniaxial pressure $p||c$. Specifically, the onset temperature of the SKL phase, at $B||c = 2.1$ T, increases by $\partial T_{\mathrm{II-III}}/\partial p_c = 8.5(1.2)$ K/GPa and the field range where it is present at 2 K widens as $\Delta B_{\mathrm{skyr}}/p_c \approx 0.07$ T/GPa.

*Contact author: klingeler@kip.uni-heidelberg.de

II. EXPERIMENTAL METHODS

All measurements were performed on two oriented cuboid-shaped single crystals of $GdRu_2Si_2$. The cuboids were cut from the same single-crystalline boule which has been grown by the floating-zone method as described in Ref. [35]. The sample dimensions and orientations were $0.590\,(||a) \times 0.801\,(||b) \times 1.182\,(||c)$ mm^3 (crystal 1) and $0.761\,(||[110]) \times 1.400\,(||[-110]) \times 3.112\,(||c)$ mm^3 (crystal 2). Magnetization measurements were performed using the vibrating sample magnetometer (VSM) option of Quantum Design's Physical Properties Measurement System (PPMS-14) and Quantum Design's Magnetic Properties Measurement System (MPMS3) in the temperature range of 2 to 300 K and in fields up to 14 and 7 T, respectively. Specific-heat data were obtained in the range of 1.8 to 300 K and with high resolution on the smaller crystal 1 used for dilatometry in the range of 1.8 to 50 K by means of a relaxation method using the PPMS. In order to account for differences in the absolute values due to mass and background errors, the latter data were scaled to the full temperature-range data at 50 K (see Fig. S1 in the Supplemental Material (SM) [41]). High-resolution dilatometric measurements were performed in two different setups, both using a three-terminal capacitance dilatometer from Küchler Innovative Measurement Technologies [42,43]. The first setup is home-built and placed in a variable temperature insert (VTI) of an Oxford Instrument magnet system [44]. The second setup is an insert provided from Küchler Innovative Measurement Technologies for the PPMS, including an option to rotate the sample up to 90°. The linear thermal expansion coefficients $\alpha_i = 1/L_\mathrm{i} \times dL_\mathrm{i}(T)/dT$ are derived from the relative length changes. Furthermore, magnetostriction, i.e., the field-induced relative length changes $dL_\mathrm{i}(B)/L_\mathrm{i}$, are obtained for fields up to 15 T at various temperatures up to 150 K and the magnetostriction coefficients $\lambda_i = 1/L_\mathrm{i} \times dL_\mathrm{i}(B)/dB$ are derived. For all dilatometric measurements, the field is aligned parallel to the measured axis.

III. RESULTS

A. Magnetic order and magnetoelastic coupling in zero magnetic field

The static magnetic susceptibility χ_i along the different crystallographic directions i follows a Curie-Weiss-like behavior down to ∼85 K, as shown in Fig. 1 as well as in Fig. S2 in the Supplemental Material (SM) [41]. The high-temperature behavior evidences an isotropic g factor as expected for Gd^{3+} systems. Upon further cooling, nonlinear behavior of χ^{-1} below about 80 K and appearance of small anisotropy indicates the evolution of short-range magnetic order. Pronounced peaks in χ_i at $T_\mathrm{N} = 45.7(5)$ K signal the onset of the long-range antiferromagnetic order. Below T_N, two additional anomalies evidence additional magnetic phase transitions at $T_1 = 44.6(5)$ K and $T_2 = 39.0(5)$ K, respectively. All observed phase transitions are of a continuous nature and are clearly visible as distinct jumps in Fisher's specific heat $\partial(\chi_\mathrm{i}T)/\partial T$ (see the inset of Fig. 1). Note that anomalies at T_N and T_2 have been observed before, while the phase transition at T_1 has not been reported [28,36,38]. Fitting the averaged static magnetic susceptibility $\chi = (2\chi_\mathrm{a} + \chi_\mathrm{c})/3$ between 200 and 300 K by means of an extended Curie-Weiss law $C/(T + \Theta) + \chi_0$ yields the effective moment $\mu_\mathrm{eff} = 8.0(2)\,\mu_\mathrm{B}$/f.u., which agrees well with previous reports [45] and matches the expected value for free Gd^{3+} moments of $7.94\,\mu_\mathrm{B}$/f.u. The obtained Weiss temperature $\Theta = 42(1)$ K indicates predominant ferromagnetic interaction in $GdRu_2Si_2$.

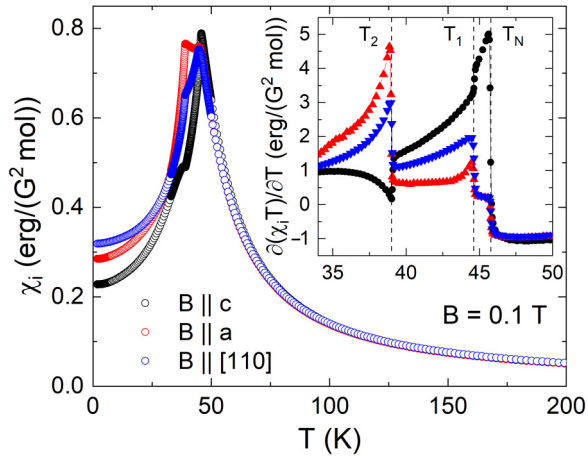

FIG. 1. Temperature dependence of the static magnetic susceptibility $\chi = M/B$ measured at $B = 0.1$ T applied along the crystallographic i axis ($i = c, a, [110]$). Inset: Fisher's specific heat $\partial(\chi_i T)/\partial T$. Dashed lines mark the anomalies at T_N, T_1, and T_2 (see the text).

The evolution of antiferromagnetic order in zero magnetic field is accompanied by pronounced anomalies in the relative length changes dL_i/L_i and in the thermal expansion coefficients α_i, as can be seen in Fig. 2. Monotonous shrinking of the c axis upon cooling, which we observe in the whole temperature regime under study up to 200 K, is superimposed by a clear kink at T_N. The corresponding thermal expansion coefficient α_c shows three positive λ-like anomalies at T_N, T_1, and T_2. This observation agrees with a previous study where, however, only one anomaly, at T_N, was observed in α_c [46]. Our data imply significant magnetoelastic coupling since the onset and changes of magnetic order are accompanied by distinct lattice changes. Similarly, there are also clear anomalies in dL_i/L_i at T_N for the a and [110] axes. Both axes show monotonous expansion upon cooling below 60 K. Again, three jumplike discontinuities can be seen in the thermal expansion coefficient $\alpha_{[110]}$, indicating the distinct phase boundaries. The associated jumps upon cooling are negative at T_N and T_1, but the one at T_2 is positive (see Fig. 2, but note the negative scaling factor). For the a axis, only two jumps are observed in α_a: a negative one at T_N and a positive one at T_2. This indicates that the dependence of T_1 on uniaxial pressure along the a axis is small so that the anomaly is not resolved in our measurement.

The Ehrenfest relation

$$\left.\frac{\partial T^*}{\partial p_i}\right|_B = T^* V_\mathrm{m} \frac{\Delta\alpha_i}{\Delta c_\mathrm{p}} \tag{1}$$

links the anomalies $\Delta\alpha_i$ and Δc_p of a continuous phase transition to the uniaxial pressure dependence of the transition temperature T^*. Hence, the signs of thermal expansion anomalies imply the respective signs of the corresponding

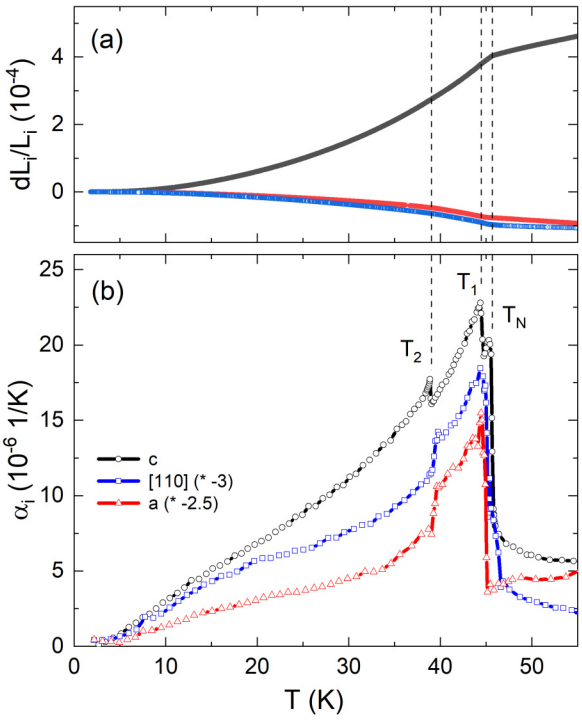

FIG. 2. (a) Relative length changes dL_i/L_i along the crystallographic c, [110], and a axes, and (b) corresponding thermal expansion coefficients α_i. For better visualisation, data for $\alpha_{[110]}$ and α_a have been multiplied by -3 and -2.5, respectively. Vertical dashed lines indicate the transition temperatures T_N, T_1, and T_2.

initial uniaxial pressure dependencies. The data in Fig. 2(b) hence signal the increase of T_N, T_1, and T_2, respectively, upon application of uniaxial pressure along the c axis, i.e., $\partial T_{N/1/2}/\partial p_c > 0$. Likewise, we read off that uniaxial pressure applied along the a and [110] axis, respectively, will yield a decrease of T_N. This result is in agreement with theoretical predictions by Bouaziz *et al.* [39], which propose a decrease of T_N when compressing the lattice along the a direction. Notably, our data show that the effect of in-plane uniaxial pressure on T_2 is opposite to the effect on T_N as both $p_{[110]}$ and p_a yield an increase of T_2 (i.e., $\partial T_2/\partial p_{a/[110]} > 0$).

To further investigate the successive ordering phenomena, the magnetic Grüneisen parameter $\gamma_i = \alpha_i^{mag}/c_p^{mag}$ is evaluated which compares the magnetic contribution to the thermal expansion coefficient α_i^{mag} and the magnetic heat capacity c_p^{mag} [47,48]. The magnetic heat capacity is determined by subtracting the phononic contribution to the heat capacity c_p^{phon} from the experimental data, i.e., $c_p^{mag} = c_p - c_p^{phon}$. In order to estimate the phononic contribution, an Einstein-Debye model with one Einstein and one Debye mode is fitted to c_p between 80 and 300 K (see Fig. S3 in the SM [41]). The model yields $\Theta_E = 598$ K and $\Theta_D = 283$ K. Calculating the resulting magnetic entropy by integrating $(c_p - c_p^{ph})/T$ yields $S_{mag} = 16.6$ J/(mol K), which is in good agreement with the expected magnetic entropy changes of a Gd^{3+} system, $S_{mag}^{theo} = R \times \ln(8) = 17.3$ J/(mol K), and confirms the reliability of the thus obtained background. The parameters Θ_i were then used to approximate the phononic contribution to the thermal expansion coefficients with the prefactors as

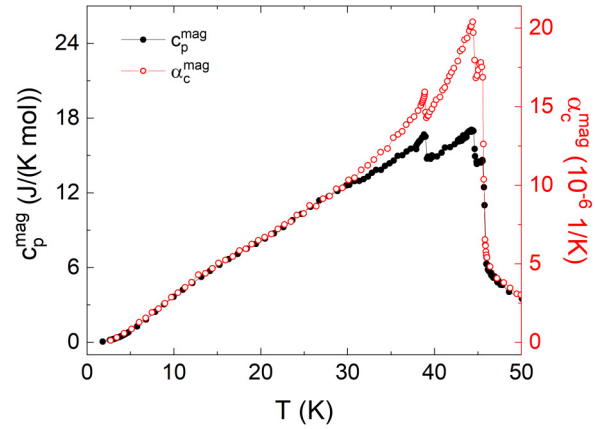

FIG. 3. Magnetic specific heat c_p^{mag} (filled black markers; left ordinate) and magnetic contribution to the thermal expansion coefficient α_c^{mag} (open red markers; right ordinate).

free fitting variables.[1] Figure 3 shows the resulting magnetic contributions of c_p and α_c scaled such that they overlap at low temperatures. Our results imply that the magnetic Grünseisen ratio is constant up to ~30 K with the Grüneisen parameter $\gamma_c = 7.9(2) \times 10^{-7}$ mol/J. We conclude the presence of a single dominant energy scale ϵ for this temperature regime, which uniaxial pressure dependence can be derived by using the Grüneisen relation [47,50],

$$\frac{\partial \ln(\epsilon)}{\partial p_i} = V_m \frac{\alpha_i}{c_p}. \tag{2}$$

Using the molecular volume $V_m = 5.02(1) \times 10^{-5}$ m^3/mol [33], applying Eq. (2) yields $\partial ln(\epsilon)/\partial p_c = 4.0(1)\%$/GPa. In contrast, Grüneisen scaling by a single parameter fails for temperatures above 30 K, up to T_N. This implies that neither in phase IV ($T_2 \leqslant T \leqslant T_1$) nor in phase VI ($T_1 \leqslant T \leqslant T_N$) is magnetic order driven by a single energy scale, but there are competing degrees of freedom in both phases. In addition, the experimental observation that Grüneisen scaling fails at $T \gtrsim 30$ K, i.e., well below T_2, implies the presence of a competing energy scale in this temperature regime of the low-temperature phase I also [51].

Comparing the jumps in the thermal expansion coefficient $\Delta\alpha_i$ and heat capacity Δc_p at the phase transitions enables us to quantify the uniaxial pressure dependence of the respective transition via the Ehrenfest relation [Eq. (1)]. For a λ-shaped anomaly, the respective jumps are superimposed by fluctuations so that the height of the jumps at the phase transition is determined by fitting lines to the data in a regime below and above the phase transition temperatures, respectively [52] (see Fig. S4 in the SM [41]). The resulting jumps in α_c and c_p, as well as the calculated uniaxial pressure dependencies for uniaxial pressure along the c axis, are listed in Table I.

B. Effect of magnetic fields $B \parallel c$ and magnetic phase diagram

Applying a magnetic field parallel to the c axis induces significant changes to the magnetic phases, as shown by the many anomalies in the thermal expansion coefficients

[1]For a detailed description of the general procedure, see Ref. [49].

TABLE I. Jumps (see text as well as Fig. S4 in the SM [41]) in the thermal expansion coefficient α_c and the heat capacity c_p at T_j ($j = N, 1, 2$), as well as the resulting uniaxial pressure dependencies calculated using the Ehrenfest relation [Eq. (1)].

	$\Delta\alpha_c$ (10^{-6} 1/K)	Δc_p (J/K/mol)	$\partial T_j/\partial p_c$ (K/GPa)
T_N	13.2(1.2)	9.2(1.2)	3.3(5)
T_1	3.3(3)	2.8(4)	2.6(4)
T_2	1.2(2)	1.9(3)	1.2(3)

α_c and Fishers' specific heat at various fields displayed in Fig. 4. In addition to the measurements at constant magnetic field, isothermal magnetostriction and magnetization data are shown in Figs. 5 and 6. The observed anomalies are used to construct the magnetic phase diagram in Figs. 8 and 9. A detailed analysis and discussion of the anomalies will be given in Secs. III C and III D.

As shown in Sec. III A, in zero magnetic field, three distinct magnetic phases are observed: phase I at $T \leqslant T_2$, phase IV at $T_2 \leqslant T \leqslant T_1$ and phase VI between T_1 and T_N (labeling of phases is done in consistency with Ref. [38]). Phase I consists of a double-Q constant moment solution, with a helix and orthogonal spin density wave propagating on the

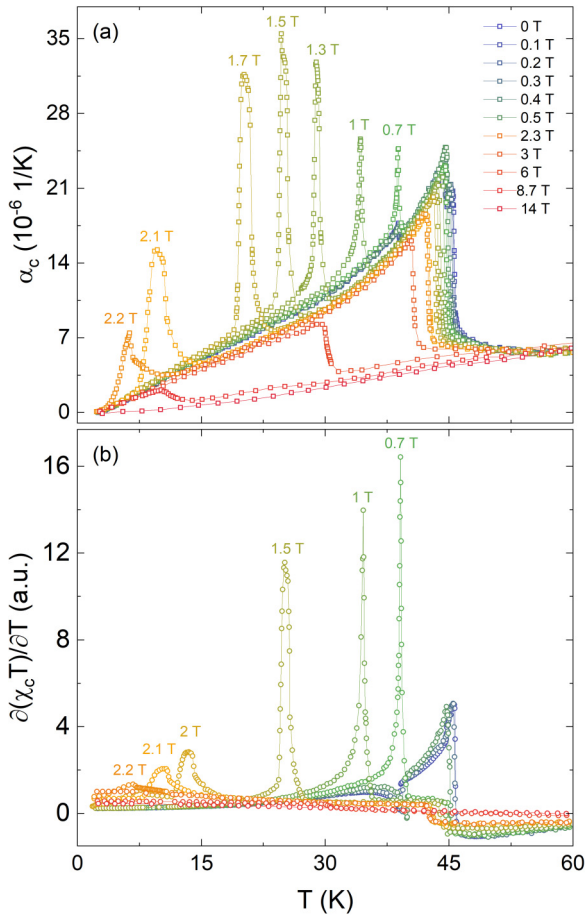

FIG. 4. (a) Linear thermal expansion coefficient α_c for various magnetic fields $B||c$ up to 14 T. (b) Fisher's specific heat $\partial(\chi_c T)/\partial T$ for various magnetic fields up to 8.7 T. For a more detailed view of each individual measurement, see Figs. S6 and S8 in the SM [41].

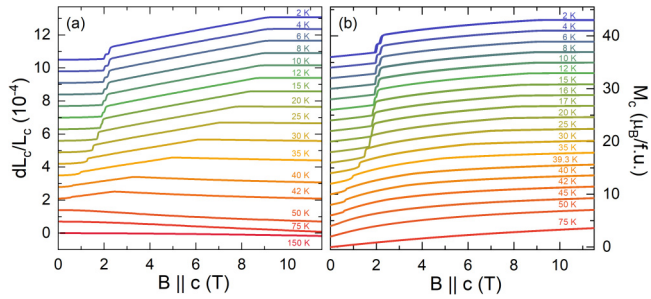

FIG. 5. (a) Magnetostriction $dL_c(B)/L_c$ and (b) isothermal magnetization M_c at various temperatures as a function of the magnetic field $B \parallel c$. For a detailed plot of the low-field region, see Figs. S9 and S11 in the SM [41].

principal magnetic propagation vectors $\mathbf{q}_1$ and $\mathbf{q}_2$; a second helix propagates along $\mathbf{q}_1 + 2\mathbf{q}_2$, which connects the arms of the star providing a constant moment solution [35,37]. Phase IV has either a sinusoidal or a helical spin structure [37]. The spin structure of phase VI is unknown. For small magnetic fields $B \parallel c$, T_N decreases while T_1 increases. Both phase boundaries merge at around 0.5 T, thereby closing phase VI, as summarized in Fig. 9. As indicated in the figure, the detailed slope of the phase boundaries around $B \simeq 0.5$ T and $T \simeq 45$ K, separating phases IV, VI (and III), are not exactly clarified by our measurements since the associated anomalies are weak and partly overlap. Similar to T_1, T_2 is shifted to higher temperatures with increasing field so that phase I is stabilized over phase IV.

At intermediate fields, anomalies in the magnetostriction and thermal expansion indicate the field-driven evolution of the square skyrmion lattice (phase II) and a fan structure (phase III). Specifically, isothermal magnetization at $T = 42$ K exhibits a jump at $B_{IV-III} = 0.58(2)$ T, signaling

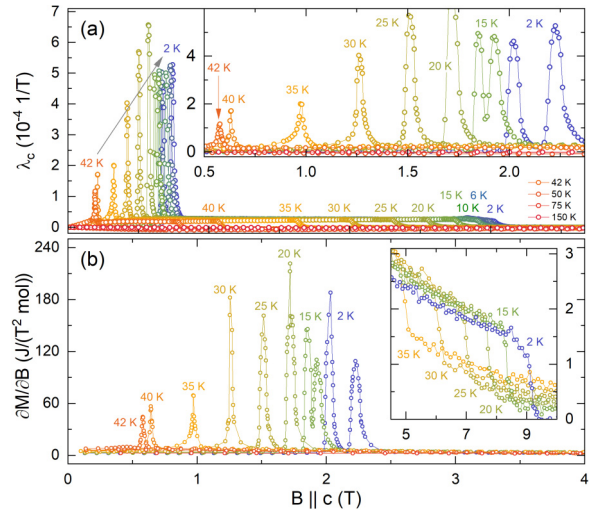

FIG. 6. (a) Magnetic field dependence of the magnetostriction coefficient λ_c for $B \parallel c$ at temperatures between 2 and 150 K. Inset: The region between 0.5 and 2.3 T in more detail. (b) Magnetic susceptibility $\partial M_c/\partial B$ at various temperatures for $B \parallel c$. Inset: The behavior at the fully polarized state in more detail. See Figs. S8 and S10 in the SM [41] for separate plots of the data.

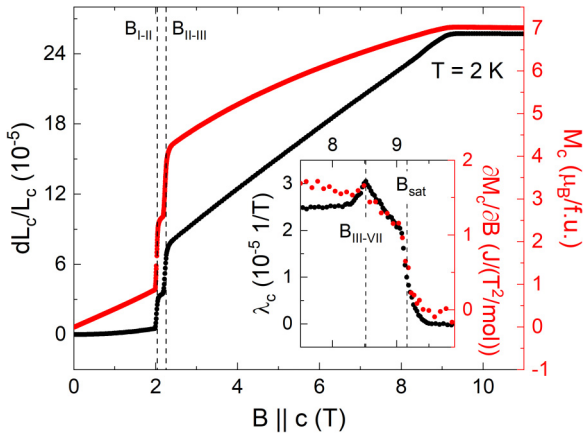

FIG. 7. Magnetostriction $dL_c(B)/L_c$ (left ordinate) and isothermal magnetization M_c (right ordinate) as a function of magnetic field $B \parallel c$ at $T = 2$ K. Inset: Magnetostriction coefficient λ_c (left ordinate) and magnetic susceptibility $\partial M_c/\partial B$ (right ordinate) around the saturation field B_{sat}. Vertical dashed lines show the transitions into and out of the skyrmion lattice phase at B_{I-II}, B_{II-III}, $B_{III-VII}$, and B_{sat}.

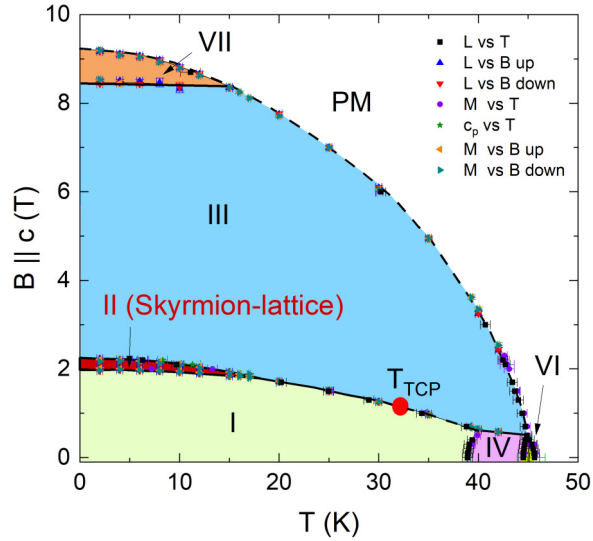

FIG. 8. Magnetic phase diagram of $GdRu_2Si_2$ for the $B||c$ axis constructed from magnetization $M(T, B)$, dilatometry $L(T, B)$, and specific-heat $c_p(T, B)$ data. Lines are guides to the eye. Solid/dashed lines represent first-/second-order phase boundaries. T_{TCP} approximates the position of the tricritical point. Phase II (red) marks the skyrmion lattice phase, PM (white) the paramagnetic phase, and phase I (green) and III (blue) are double-Q states. The spin configurations in phases IV (purple), VI (yellow) and VII (orange) have not been investigated yet.

a first-order phase transition from phase IV to III. Similarly, dilatometric and magnetic measurements at $T \geqslant 20$ K and in fields between ∼0.7 and ∼2 T enable us to investigate the phase boundary between phases I and III. Notably, the associated anomalies qualitatively change with decreasing temperature, which implies that the nature of the phase transition changes from a continuous character to a discontinuous one upon cooling. This is seen in λ_c and $\partial M_c/\partial B$, which show a λ-like behavior at 35 and 40 K (see Fig. 6). Concomitantly, λ-like anomalies are also visible in α_c and $\partial(\chi T)/\partial T$ at 1 T and 0.7 T [Fig. 4 and Figs. 10(a), 10(b)]. With decreasing temperature, however, the λ-like character of the magnetostriction anomaly vanishes and becomes more symmetric until it is undoubtedly symmetric around 25 K [Fig. 6(a)]. In the temperature-dependent measurements, the anomaly in α_c loses its λ shape between 1 and 1.3 T, thereby further validating the observation in the isothermal studies. The symmetric peaks imply jumps in the c-axis length and in the magnetization, i.e., they prove the first-order nature of the phase transition in this region of the phase diagram. Our observations hence imply the presence of a tricritical point on the phase boundary between phases I and III at ∼33 K.

Below about 20 K, the evolution of the skyrmion lattice phase II is evidenced by the appearance of two subsequent jumps in magnetostriction and isothermal magnetization, signaling the discontinuous phase boundaries I-II and II-III. The behavior at $T = 2$ K is shown in detail in Fig. 7, which shows that phase II extends from $B_{I-II}(2\text{ K}) = 2.02(2)$ T to $B_{II-III}(2\text{ K}) = 2.23(2)$ T, with B_{I-II} and B_{II-III} being the critical fields of the phase transition from phase I to II and phase II to III, respectively.[2] Both critical fields show hysteretic behavior, which further illustrates the discontinuous character of the phase boundaries (see Figs. S10 and S12 in the SM [41]) with a field hysteresis ∼0.05(1) T. Upon heating, the skyrmion lattice phase is suppressed by phase III and becomes narrower for higher temperatures (see Fig. 8).

The transition temperature from the PM phase into the fan structure phase III is continuously suppressed in external magnetic fields as expected for an antiferromagnetically ordered state. In contrast to previously reported phase diagrams [28,35,38], phase III, however, does not extend to the highest field since we observe a novel phase VII below about 15 K. The phase boundary III-VII is nearly temperature

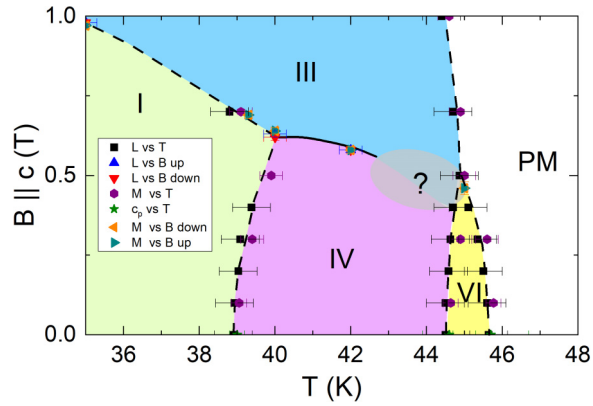

FIG. 9. Magnetic phase diagram for $B||c$ in more detail around T_N (see Fig. 8). The exact positions of the boundaries between phases III, IV, and VI at $B||c \simeq 0.5$ T cannot be precisely determined by our data.

[2]Similar behavior is reported in Ref. [46], where magnetostriction shows two consecutive but smeared-out anomalies. The measurement temperature in Ref. [46] is not specified, but the reported data suggest $T < 10$ K.

independent, as evidenced by a peak in λ_c and $\partial M_c/\partial B$ at $B_{\mathrm{III-VII}} \simeq 8.5$ T. The observed symmetric anomaly (see inset, Fig. 7) indicates a first-order phase transition, as also illustrated by the small hysteresis shown in Figs. S10 and S12 in the SM [41]. The respective jumps at $T = 2$ K in $\Delta L_c/L_c$ and ΔM amount to $1.9(5) \times 10^{-6}$ and $3.9(9) \times 10^{-3}$ μ_B/f.u., respectively. Finally, at 2 K, the fully polarized phase is reached above ~9.3 T (cf. Fig. 8).

C. Uniaxial pressure effects on the skyrmion lattice phase

The response of the skyrmion lattice phase to uniaxial pressure can be deduced from the jumplike features in the data and quantified via Clausius-Clapeyron equations (e.g., [53]). For constant temperature, the equations yield the dependence of the transition field B^* on uniaxial pressure applied along the i axis from the associated jumps in the length ΔL_i and in the magnetization $\Delta M_{B||i}$,

$$\left.\frac{\partial B^*}{\partial p_i}\right|_T = V_m \frac{\Delta L_i/L_i}{\Delta M_{B||i}}. \quad (3)$$

Analogously, when measuring at constant magnetic field B, the ratio of the jumps in the length ΔL_i and the entropy jump ΔS yield the uniaxial pressure dependence of the ordering temperature $T^*(B)$,

$$\left.\frac{\partial T^*}{\partial p_i}\right|_B = V_m \frac{\Delta L_i/L_i}{\Delta S}. \quad (4)$$

For our analysis, we deduce the ΔS from the slope of the phase boundary at constant pressure at the respective magnetic field by exploiting $\Delta S = -\Delta M_{B||i}/(\partial T^*/\partial B|_p)$. This finally yields

$$\left.\frac{\partial T^*}{\partial p_i}\right|_B = -V_m \left.\frac{\partial T^*}{\partial B}\right|_p \frac{\Delta L_i/L_i}{\Delta M_{B||i}}. \quad (5)$$

Similarly to the above-mentioned procedure to determine anomaly sizes, we have extracted the jumps ΔL_c and $\Delta M_{B||c}$ from the experimental data by fitting lines to the data well below and above the anomalies. The resulting jumps and calculated uniaxial pressure dependencies obtained from the isothermal measurements at the phase boundaries into the SKL phase (I-II, i.e., $B_{\mathrm{I-II}}$) and out of the SKL phase (II-III; $B_{\mathrm{II-III}}$) are displayed in Table S1 in the SM [41]. The calculated uniaxial pressure dependencies for the respective phase boundaries exhibit no significant changes with temperature, being $\partial B_{\mathrm{I-II}}/\partial p_c \simeq 0.17$ T/GPa and $\partial B_{\mathrm{II-III}}/\partial p_c \simeq 0.24$ T/GPa on average.

Furthermore, by extracting the slope of the respective phase boundary $\partial T_j/\partial B$ (j = I-II, II-III), the pressure dependency of the transition temperature $\partial T_j/\partial p_c$ can be calculated using Eq. (5) and values from Table S1 in the SM [41]. Specifically, $\partial T_j/\partial B$ was approximated by fitting a polynomial to the respective phase boundary and determining the field derivative. Table S2 in the SM [41] lists the approximated slopes of the respective phase boundaries and the obtained uniaxial pressure dependencies. For both phase boundaries I-II and II-III, the uniaxial pressure dependencies of the transition temperatures $T_{\mathrm{I-II}}$ and $T_{\mathrm{II-III}}$ are positive, being of the order of 10 K/GPa. Furthermore, for both boundaries, $\partial T_j/\partial p_c$ increases for higher magnetic fields, which can be mostly attributed to the increasing slope of the phase boundary $\partial T_j/\partial B$.

TABLE II. Uniaxial pressure dependencies of the phase boundaries j shown in Fig. 8 for $p||c$. The presented values are from calculations using the Clausius-Clapeyron and Ehrenfest relations [see Eqs. (1), (5), and (3)]. Values marked with an asterisk have been obtained from phase boundaries where more than one value could be calculated. In these cases, the averages are taken and the error bars include the variations at the phase boundary. If no quantitative values can be obtained, the sign of the pressure dependence is given.

Phase boundary j	$\partial B_j/\partial p_c$ (T/GPa)	$\partial T_j/\partial p_c$ (K/GPa)
I-IV	+	1.2(3)
IV-VI	+	2.6(4)
VI-PM	+	3.3(3)
I-III (first order)	0.20(4)*	4.5(6)
I-III (second order)	0.13(3)*	+
IV-III	0.11(2)	+
III-PM	+	+
I-II	0.17(3)*	20(−13,+60)*
II-III	0.24(3)*	15(−11,+40)*
III-VII	4.3(1.5)	+
VII-PM	+	+

D. Discussion

The phase diagram in Fig. 8 shows the presence of six distinct ordered phases evolving below T_N in external magnetic fields B applied along the crystallographic c axis. Similar to the analysis of thermal expansion and magnetostriction anomalies at the boundaries of the SKL phase, the data in Figs. 2–6, as well as further data presented in the SM [41] imply the dependencies of the respective ordering phenomena upon application of uniaxial pressure along the c axis (p_c). The results are summarized in Table II and, interestingly, show only positive values for the uniaxial pressure dependencies. This implies that phase I is stabilized over all adjacent phases II–IV in temperature and magnetic field. Phases IV and VI, the remaining zero-field phases, are both shifted to higher temperatures (see Fig. 9) and span over a larger temperature interval for $p||c$ since $\partial T_{\mathrm{I-IV}}/\partial p_c < \partial T_{\mathrm{IV-VI}}/\partial p_c < \partial T_{\mathrm{VI-PM}}/\partial p_c$. Furthermore, phase IV is stabilized over phase III under uniaxial pressure p_c. As already discussed above, the skyrmion lattice phase shifts to higher fields and widens in magnetic field. Also, phases III and VII are stabilized towards higher temperatures and magnetic fields upon applying the $p||c$ axis. Notably, phase VII is particularly sensitive to p_c as $\partial B_{\mathrm{III-VII}}/\partial p_c$ is two orders of magnitude larger than the pressure dependencies of all other phase boundaries. It is of the order of 5 T/GPa, implying that phase VII is strongly suppressed in favor of phase III.

Pressure effects on the skyrmion lattice phase are of particular interest as they provide further insight into the microscopic mechanism stabilizing this phase. The observed uniaxial pressure dependencies of the phase boundaries enclosing the skyrmion lattice phase are all positive, i.e., uniaxial pressure along the c axis stabilizes the skyrmion lattice towards higher fields and temperatures. Furthermore, for all

measured temperatures, $\partial B_{\mathrm{II-III}}/\partial p_c$ is larger than $\partial B_{\mathrm{I-II}}/\partial p_c$ so that the skyrmion lattice phase also widens in magnetic field at an approximate rate of $\Delta B_{\mathrm{skyr}}/p_c \approx 0.07$ T/GPa. An enhancement of the skyrmion lattice phase under uniaxial pressure is also observed in materials such as Gd_2PdSi_3 [54], Cu_2OSeO_3 [55], and MnSi [56]. Especially interesting for comparison is Gd_2PdSi_3, which also crystallizes in a centrosymmetric structure and is predominantly governed by RKKY interactions [24]. Similar to the present case, the SKL phase widens in magnetic field in Gd_2PdSi_3 for uniaxial pressure parallel to the c axis at approximately half the rate compared to $GdRu_2Si_2$. However, for Gd_2PdSi_3, the sign of pressure dependence is opposite so that the SKL phase shifts towards lower magnetic fields. The pressure dependence of the critical fields is weaker by approximately one order of magnitude in Gd_2PdSi_3 compared to $GdRu_2Si_2$ [54]. In contrast to the strongly differing pressure dependencies of the critical fields, the ordering temperatures of the SKL phases in both materials' change are of similar magnitude; however, again, with opposite sign: while in Gd_2PdSi_3, $\partial T_{\mathrm{skyr}}/\partial p_c = -6.1$ K/GPa, in $GdRu_2Si_2$, we find $\partial T_{\mathrm{skyr}}/\partial p_c \simeq +15$ K/GPa (see Table II). In the case of the two noncentrosymmetric systems, Cu_2OSeO_3 and MnSi, the respective SKL phases also widen in magnetic field under pressure [55,56]. Moreover, the SKL phase in MnSi shows the general shift towards higher fields, while for Cu_2OSeO_3, the SKL phase extends towards higher temperatures, as observed for $GdRu_2Si_2$.

While uniaxial pressure effects on all ordered phases are always positive, the effect of external magnetic fields $B||c$ differs for the various phases, not only quantitatively but also with respect to its sign. At low magnetic field $B \lesssim 0.5$ T, phases I and IV are stabilized over their respective higher-temperature phases, i.e., the phase boundaries show positive slope $\partial T_1/\partial B_c > 0$ and $\partial T_2/\partial B_c > 0$ (see Fig. 9). Thermodynamically, this is associated with an increase of magnetization or its derivative upon cooling at the respective phase boundaries, which is indeed observed in the magnetization data in Fig. 1. All other phase boundaries show negative slopes, i.e., the underlying magnetic orders are suppressed by $B||c$ (see Fig. 8).

Our results show that phase VII forms a pocket at high fields and low temperatures, with an upper boundary to the fully polarized state; $B_{\mathrm{sat}}(T)$ is very similar to what would be expected for phase III (cf. Fig. 8). While the phase boundary $B_{\mathrm{III-VII}}(T)$ is nearly temperature independent, it displays a comparably giant uniaxial pressure dependence so that phase VII will be fully suppressed by applying p_c of a few tenths of GPa. By means of the Clausius-Clapeyron equation, we obtain an upper limit of the entropy changes of $\Delta S_{\mathrm{III-VII}}(T = 2\ \mathrm{K}) < 5 \times 10^{-4}$ J/(mol K), which uses the observed jump in M and the tiny slope ($\ll$0.1 T/K) of the phase boundary at the respective transition. The spin structure of phase VII has not been investigated yet. First-principles numerical studies by Bouaziz *et al.* [39], however, may reveal a possible nature of this phase. Their calculations for $GdRu_2Si_2$ predict that in the fully polarized state close to the boundary of the cycloidal phase (phase III), single metastable skyrmions emerge. One might speculate whether such skyrmions form a superstructure which could be our observed phase VII. If so, it is very sensitive to and easily suppressed by pressure p_c, while entropically it is very similar to phase III.

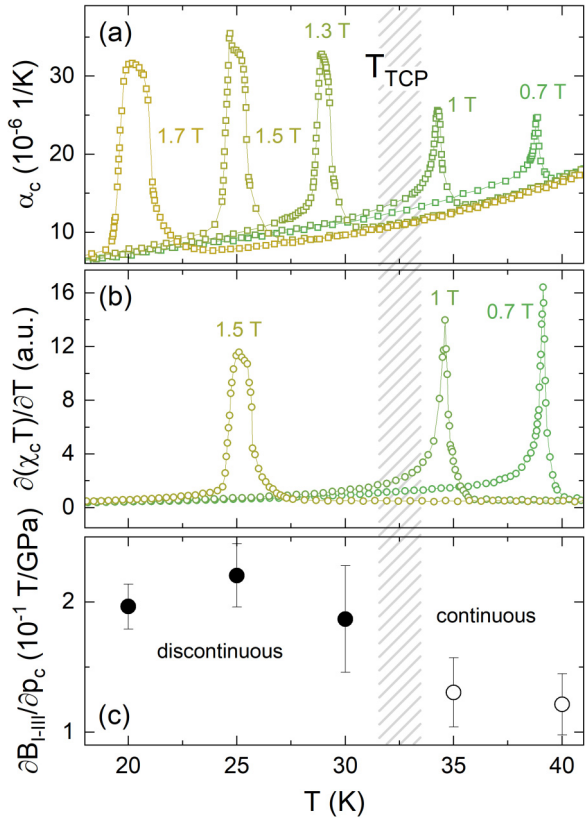

FIG. 10. Anomalies associated with the phase transition between phases I and III in (a) the linear thermal expansion coefficient α_c and (b) Fisher's specific heat $\partial(\chi_c T)/\partial T$. (c) Uniaxial pressure dependence $\partial B_{\mathrm{I-III}}/\partial p_c$ at the phase boundary I-III. The dashed region marks the temperature regime of the tricritical point.

We finally discuss the phase boundary between phases I and III which, as mentioned above, displays a continuous nature above 35 K, as demonstrated by textbooklike anomalies at $B_{\mathrm{I-III}}$, while we observe first-order discontinuities in M and L below 25 K (see Figs. 4 and 5). The evolution of the anomaly shape along the phase boundary is illustrated in Figs. 10(a) and 10(b), which shows the change from asymmetric and clearly λ-shaped anomalies (confirming the continuous nature of the transition) for $T > T_{\mathrm{TCP}}$ to rather symmetric anomalies with sharp low-temperature flanks (indicating the first-order character of the boundary) in α_c and $\partial(\chi_c T)/\partial T$ for $T < T_{\mathrm{TCP}}$. Our findings suggest the existence of a tricritical point (TCP) at $T_{\mathrm{TCP}} \simeq 33$ K (see Fig. 8), i.e., well above the triple point where the SKL evolves in between phases I and III. The existence of a TCP is further supported by the temperature dependence of the uniaxial pressure dependence of $B_{\mathrm{I-III}}(T)$ presented in Fig. 10(c). Above and below T_{TCP}, the uniaxial pressure dependence of the critical field $\partial B_{\mathrm{I-III}}/\partial p_c$ is fairly constant, but its value changes by about 40% at T_{TCP}. Overall, the continuous transition between double-Q magnetic structures in phases I and III evolves a discontinuous character upon cooling [see Figs. 10(a) and 10(b)] before the SKL phase evolves upon further cooling at $T_{\mathrm{tri}} \simeq 18\ \mathrm{K} < \mathrm{T_{TCP}}$. This behavior shows slight similarities, but essentially contrasts

to findings in the skyrmion lattice systems MnSi [57,58], Cu_2OSeO_3 [59], and GaV_4S_8 [60], where tricritical behavior is reported only at triple points of the phase diagram. In all three examples, the TCP appears at a phase boundary towards the fully polarized phase which, in the case of the skyrmion-pocket phases in MnSi and Cu_2OSeO_3, does not involve a phase boundary towards the skyrmion phase, while only in GaV_4S_8 [60] the TCP edges the SKL phase.

IV. SUMMARY

We report high-resolution capacitance dilatometry, specific-heat, and magnetization studies which are used to complete the magnetic phase diagram in $GdRu_2Si_2$. We observe three successive antiferromagnetic phases in zero magnetic field (phases I, IV, VI), with phase VI not reported and of unknown structure. In addition, we also find a high-field phase (phase VII), which features a comparably giant uniaxial pressure dependence. By means of our dilatometric data, we determine magnetoelastic effects as well as uniaxial pressure dependencies of the various phases. The skyrmion lattice phase is enhanced towards higher fields and temperatures and widens at a rate of 0.07 T/GPa when uniaxial pressure is applied along the c axis. Notably, the SKL pocket phase evolves through a triple point T_{tri} from a phase boundary between the double-Q magnetic structures in phases I and III, which, in addition, indicates a tricritical point at $T_{\mathrm{TCP}} \simeq 33\ \mathrm{K} > \mathrm{T_{tri}} \simeq 18\ \mathrm{K}$, thereby highlighting the relevance of critical fluctuations for the evolution of the skyrmion lattice phase in $GdRu_2Si_2$.

ACKNOWLEDGMENTS

We acknowledge valuable experimental advice for the specific-heat studies at the University of Warwick by Prof. Martin Lees. Support by Deutsche Forschungsgemeinschaft (DFG) under Germany's Excellence Strategy Grant No. EXC2181/1-390900948 (the Heidelberg STRUCTURES Excellence Cluster) is gratefully acknowledged. L.G. acknowledges funding by the International Max-Planck Research School for Quantum Dynamics (IMPRS-QD) Heidelberg. The work at the University of Warwick was supported by EPSRC, UK through Grants No. EP/T005963/1 and No. EP/N032128/1.

[1] T. Skyrme, A nonlinear field theory, Proc. R. Soc. London A **260**, 127 (1961).
[2] T. Skyrme, A unified field theory of mesons and baryons, Nucl. Phys. **31**, 556 (1962).
[3] A. N. Bogdanov and D. A. Yablonskii, Thermodynamically stable "vortices" in magnetically ordered crystals. The mixed state of magnets, Zh. Eksp. Teor. Fiz. **95**, 178 (1989) [Sov. Phys. JETP **68**, 101 (1989)].
[4] N. Nagaosa and Y. Tokura, Topological properties and dynamics of magnetic skyrmions, Nature Nanotech. **8**, 899 (2013).
[5] F. Büttner, C. Moutafis, M. Schneider, B. Krüger, C. M. Günther, J. Geilhufe, C. v. K. Schmising, J. Mohanty, B. Pfau, S. Schaffert, A. Bisig, M. Foerster, T. Schulz, C. A. F. Vaz, J. H. Franken, H. J. M. Swagten, M. Kläui, and S. Eisebitt, Dynamics and inertia of skyrmionic spin structures, Nat. Phys. **11**, 225 (2015).
[6] J. Iwasaki, M. Mochizuki, and N. Nagaosa, Current-induced skyrmion dynamics in constricted geometries, Nat. Nanotechnol. **8**, 742 (2013).
[7] M. Lee, W. Kang, Y. Onose, Y. Tokura, and N. P. Ong, Unusual Hall effect anomaly in MnSi under pressure, Phys. Rev. Lett. **102**, 186601 (2009).
[8] G. Yin, Y. Liu, Y. Barlas, J. Zang, and R. K. Lake, Topological spin Hall effect resulting from magnetic skyrmions, Phys. Rev. B **92**, 024411 (2015).
[9] M. Leroux, M. J. Stolt, S. Jin, D. V. Pete, C. Reichhardt, and B. Maiorov, Skyrmion lattice topological Hall effect near room temperature, Sci. Rep. **8**, 15510 (2018).
[10] C. Hanneken, F. Otte, A. Kubetzka, B. Dupé, N. Romming, K. von Bergmann, R. Wiesendanger, and S. Heinze, Electrical detection of magnetic skyrmions by tunnelling non-collinear magnetoresistance, Nat. Nanotechnol. **10**, 1039 (2015).
[11] D. Prychynenko, M. Sitte, K. Litzius, B. Krüger, G. Bourianoff, M. Kläui, J. Sinova, and K. Everschor-Sitte, Magnetic skyrmion as a nonlinear resistive element: A potential building block for reservoir computing, Phys. Rev. Appl. **9**, 014034 (2018).
[12] K. M. Song, J.-S. Jeong, B. Pan, X. Zhang, J. Xia, S. Cha, T.-E. Park, K. Kim, S. Finizio, J. Raabe, J. Chang, Y. Zhou, W. Zhao, W. Kang, H. Ju, and S. Woo, Skyrmion-based artificial synapses for neuromorphic computing, Nat. Electron. **3**, 148 (2020).
[13] T. Yokouchi, S. Sugimoto, B. Rana, S. Seki, N. Ogawa, Y. Shiomi, S. Kasai, and Y. Otani, Pattern recognition with neuromorphic computing using magnetic field-induced dynamics of skyrmions, Sci. Adv. **8**, eabq5652 (2022).
[14] S. Luo and L. You, Skyrmion devices for memory and logic applications, APL Mater. **9**, 050901 (2021).
[15] W. Koshibae, Y. Kaneko, J. Iwasaki, M. Kawasaki, Y. Tokura, and N. Nagaosa, Memory functions of magnetic skyrmions, Jpn. J. Appl. Phys. **54**, 053001 (2015).
[16] G. Yu, P. Upadhyaya, Q. Shao, H. Wu, G. Yin, X. Li, C. He, W. Jiang, X. Han, P. K. Amiri, and K. L. Wang, Room-temperature skyrmion shift device for memory application, Nano Lett. **17**, 261 (2017).
[17] S. Luo, M. Song, X. Li, Y. Zhang, J. Hong, X. Yang, X. Zou, N. Xu, and L. You, Reconfigurable skyrmion logic gates, Nano Lett. **18**, 1180 (2018).
[18] X. Zhang, M. Ezawa, and Y. Zhou, Magnetic skyrmion logic gates: Conversion, duplication and merging of skyrmions, Sci. Rep. **5**, 9400 (2015).
[19] N. Sisodia, J. Pelloux-Prayer, L. D. Buda-Prejbeanu, L. Anghel, G. Gaudin, and O. Boulle, Programmable skyrmion logic gates based on skyrmion tunneling, Phys. Rev. Appl. **17**, 064035 (2022).
[20] S. Mühlbauer, B. Binz, F. Jonietz, C. Pfleiderer, A. Rosch, A. Neubauer, R. Georgii, and P. Böni, Skyrmion lattice in a chiral magnet, Science **323**, 915 (2009).
[21] S. Seki, X. Z. Yu, S. Ishiwata, and Y. Tokura, Observation of skyrmions in a multiferroic material, Science **336**, 198 (2012).

[22] I. Kézsmárki, S. Bordács, P. Milde, E. Neuber, L. M. Eng, J. S. White, H. M. Rønnow, C. D. Dewhurst, M. Mochizuki, K. Yanai, H. Nakamura, D. Ehlers, V. Tsurkan, and A. Loidl, Néel-type skyrmion lattice with confined orientation in the polar magnetic semiconductor GaV_4S_8, Nat. Mater. **14**, 1116 (2015).

[23] X. Z. Yu, Y. Onose, N. Kanazawa, J. H. Park, J. H. Han, Y. Matsui, N. Nagaosa, and Y. Tokura, Real-space observation of a two-dimensional skyrmion crystal, Nature (London) **465**, 901 (2010).

[24] T. Kurumaji, T. Nakajima, M. Hirschberger, A. Kikkawa, Y. Yamasaki, H. Sagayama, H. Nakao, Y. Taguchi, T.-H. Arima, and Y. Tokura, Skyrmion lattice with a giant topological Hall effect in a frustrated triangular-lattice magnet, Science **365**, 914 (2019).

[25] M. Hirschberger, T. Nakajima, S. Gao, L. Peng, A. Kikkawa, T. Kurumaji, M. Kriener, Y. Yamasaki, H. Sagayama, H. Nakao, K. Ohishi, K. Kakurai, Y. Taguchi, X. Yu, T.-H. Arima, and Y. Tokura, Skyrmion phase and competing magnetic orders on a breathing kagomé lattice, Nat. Commun. **10**, 5831 (2019).

[26] R. Takagi, N. Matsuyama, V. Ukleev, Le Yu, J. S. White, S. Francoual, J. R. L. Mardegan, S. Hayami, H. Saito, K. Kaneko, K. Ohishi, Y. Ōnuki, T.-H. Arima, Y. Tokura, T. Nakajima, and S. Seki, Square and rhombic lattices of magnetic skyrmions in a centrosymmetric binary compound, Nat. Commun. **13**, 1472 (2022).

[27] N. D. Khanh, T. Nakajima, X. Yu, S. Gao, K. Shibata, M. Hirschberger, Y. Yamasaki, H. Sagayama, H. Nakao, L. Peng, K. Nakajima, R. Takagi, T.-H. Arima, Y. Tokura, and S. Seki, Nanometric square skyrmion lattice in a centrosymmetric tetragonal magnet, Nat. Nanotechnol. **15**, 444 (2020).

[28] Y. Yasui, C. J. Butler, N. D. Khanh, S. Hayami, T. Nomoto, T. Hanaguri, Y. Motome, R. Arita, T.-H. Arima, Y. Tokura, and S. Seki, Imaging the coupling between itinerant electrons and localised moments in the centrosymmetric skyrmion magnet $GdRu_2Si_2$, Nat. Commun. **11**, 5925 (2020).

[29] A. O. Leonov and M. Mostovoy, Multiply periodic states and isolated skyrmions in an anisotropic frustrated magnet, Nat. Commun. **6**, 8275 (2015).

[30] T. Okubo, S. Chung, and H. Kawamura, Multiple-Q states and the skyrmion lattice of the triangular-lattice Heisenberg antiferromagnet under magnetic fields, Phys. Rev. Lett. **108**, 017206 (2012).

[31] S. Hayami, R. Ozawa, and Y. Motome, Effective bilinear-biquadratic model for noncoplanar ordering in itinerant magnets, Phys. Rev. B **95**, 224424 (2017).

[32] K. Hiebl, C. Horvath, P. Rogl, and M. J. Sienko, Magnetic properties and structural chemistry of ternary silicides (Re, Th, U)Ru_2Si_2 (Re = RARE EARTH), J. Magn. Magn. Mater. **37**, 287 (1983).

[33] I. Felner and I. Nowik, Itinerant and local magnetism, superconductivity and mixed valency phenomena in RM_2Si_2, (R = rare earth, M = Rh, Ru)°, J. Phys. Chem. Solids **45**, 419 (1984).

[34] M. Ślaski, A. Szytuła, J. Leciejewicz, and A. Zygmunt, Magnetic properties of $ReRu_2Si_2$ (RE=Pr, Nd, Gd, Tb, Dy, Er) intermetallics, J. Magn. Magn. Mater. **46**, 114 (1984).

[35] G. D. A. Wood, D. D. Khalyavin, D. A. Mayoh, J. Bouaziz, A. E. Hall, S. J. R. Holt, F. Orlandi, P. Manuel, S. Blügel, J. B. Staunton, O. A. Petrenko, M. R. Lees, and G. Balakrishnan, Double-Q ground state with topological charge stripes in the centrosymmetric skyrmion candidate $GdRu_2Si_2$, Phys. Rev. B **107**, L180402 (2023).

[36] A. Garnier, D. Gignoux, N. Iwata, D. Schmitt, T. Shigeoka, and F. Y. Zhang, Anisotropic metamagnetism in $GdRu_2Si_2$, J. Magn. Magn. Mater. **140–144**, 899 (1995).

[37] J. A. M. Paddison, J. Bouaziz, A. F. May, Q. Zhang, S. Calder, D. Abernathy, J. B. Staunton, S. Blügel, and A. D. Christianson, arXiv:2406.04524.

[38] N. D. Khanh, T. Nakajima, S. Hayami, S. Gao, Y. Yamasaki, H. Sagayama, H. Nakao, R. Takagi, Y. Motome, Y. Tokura, T.-H. Arima, and S. Seki, Zoology of multiple-Q spin textures in a centrosymmetric tetragonal magnet with itinerant electrons, Adv. Sci. **9**, e2105452 (2022).

[39] J. Bouaziz, E. Mendive-Tapia, S. Blügel, and J. B. Staunton, Fermi-surface origin of skyrmion lattices in centrosymmetric rare-earth intermetallics, Phys. Rev. Lett. **128**, 157206 (2022).

[40] S. V. Eremeev, D. Glazkova, G. Poelchen, A. Kraiker, K. Ali, A. V. Tarasov, S. Schulz, K. Kliemt, E. V. Chulkov, V. S. Stolyarov, A. Ernst, C. Krellner, D. Y. Usachov, and D. V. Vyalikh, Insight into the electronic structure of the centrosymmetric skyrmion magnet $GdRu_2Si_2$, Nanoscale Adv. **5**, 6678 (2023).

[41] See Supplemental Material at http://link.aps.org/supplemental/10.1103/PhysRevB.111.064419, which lists the anomaly sizes, pressure, and field dependencies at the different phase boundaries. In addition, it contains further detailed data of magnetization, thermal expansion, and magnetostriction and illustrates how the anomaly sizes have been extracted from the experimental data.

[42] R. Küchler, T. Bauer, M. Brando, and F. Steglich, A compact and miniaturized high resolution capacitance dilatometer for measuring thermal expansion and magnetostriction, Rev. Sci. Instrum. **83**, 095102 (2012).

[43] R. Küchler, A. Wörl, P. Gegenwart, M. Berben, B. Bryant, and S. Wiedmann, The world's smallest capacitive dilatometer, for high-resolution thermal expansion and magnetostriction in high magnetic fields, Rev. Sci. Instrum. **88**, 083903 (2017).

[44] J. Werner, W. Hergett, M. Gertig, J. Park, C. Koo, and R. Klingeler, Anisotropy-governed competition of magnetic phases in the honeycomb quantum magnet $Na_3Ni_2SbO_6$ studied by dilatometry and high-frequency ESR, Phys. Rev. B **95**, 214414 (2017).

[45] T. Samanta, I. Das, and S. Banerjee, Comparative studies of magnetocaloric effect and magnetotransport behavior in $GdRu_2Si_2$ compound, J. Appl. Phys. **104**, 123901 (2008).

[46] J. Prokleška, J. Vejpravová, and V. Sechovský, Magnetostriction measurement of $GdRu_2Si_2$ single crystal, J. Phys.: Conf. Ser. **51**, 127 (2006).

[47] P. Gegenwart, Grüneisen parameter studies on heavy fermion quantum criticality, Rep. Prog. Phys. **79**, 114502 (2016).

[48] M. Hoffmann, K. Dey, J. Werner, R. Bag, J. Kaiser, H. Wadepohl, Y. Skourski, M. Abdel-Hafiez, S. Singh, and R. Klingeler, Magnetic phase diagram, magnetoelastic coupling, and Grüneisen scaling in $CoTiO_3$, Phys. Rev. B **104**, 014429 (2021).

[49] S. Spachmann, P. Berdonosov, M. Markina, A. Vasiliev, and R. Klingeler, Linear magnetoelastic coupling and

magnetic phase diagrams of the buckled-kagomé antiferromagnet $Cu_3Bi(SeO_3)_2O_2Cl$, Sci. Rep. **12**, 7383 (2022).

[50] R. Klingeler, J. Geck, S. Arumugam, N. Tristan, P. Reutler, B. Büchner, L. Pinsard-Gaudart, and A. Revcolevschi, Pressure-induced melting of the orbital polaron lattice in $La_{1-x}Sr_xMnO_3$, Phys. Rev. B **73**, 214432 (2006).

[51] J. Werner, S. Sauerland, C. Koo, C. Neef, A. Pollithy, Y. Skourski, and R. Klingeler, High magnetic field phase diagram and failure of the magnetic Grüneisen scaling in $LiFePO_4$, Phys. Rev. B **99**, 214432 (2019).

[52] R. Küchler, Thermische Ausdehnung und divergierendes Grüneisenverhältnis in Schwere-Fermionen-Systemen, Ph.D. thesis, Technische Universität Dresden, Dresden, 2005.

[53] U. Stockert, N. Leps, L. Wang, G. Behr, S. Wurmehl, B. Büchner, and R. Klingeler, Pr magnetism and its interplay with the Fe spin-density wave in $PrFeAsO_{1-x}F_x(x = 0, 0.15)$, Phys. Rev. B **86**, 144407 (2012).

[54] S. Spachmann, A. Elghandour, M. Frontzek, W. Löser, and R. Klingeler, Magnetoelastic coupling and phases in the skyrmion lattice magnet Gd_2PdSi_3 discovered by high-resolution dilatometry, Phys. Rev. B **103**, 184424 (2021).

[55] I. Levatić, P. Popčević, V. Šurija, A. Kruchkov, H. Berger, A. Magrez, J. S. White, H. M. Rønnow, and I. Živković, Dramatic pressure-driven enhancement of bulk skyrmion stability, Sci. Rep. **6**, 21347 (2016).

[56] A. Chacon, A. Bauer, T. Adams, F. Rucker, G. Brandl, R. Georgii, M. Garst, and C. Pfleiderer, Uniaxial pressure dependence of magnetic order in mnsi, Phys. Rev. Lett. **115**, 267202 (2015).

[57] A. Bauer, M. Garst, and C. Pfleiderer, Specific heat of the skyrmion lattice phase and field-induced tricritical point in MnSi, Phys. Rev. Lett. **110**, 177207 (2013).

[58] L. Zhang, D. Menzel, C. Jin, H. Du, M. Ge, C. Zhang, L. Pi, M. Tian, and Y. Zhang, Critical behavior of the single-crystal helimagnet MnSi, Phys. Rev. B **91**, 024403 (2015).

[59] H. C. Chauhan, B. Kumar, J. K. Tiwari, and S. Ghosh, Multiple phases with a tricritical point and a Lifshitz point in the skyrmion host Cu_2OSeO_3, Phys. Rev. B **100**, 165143 (2019).

[60] B. Liu, Z. Wang, Y. Zou, S. Zhou, H. Li, J. Xu, L. Zhang, J. Xu, M. Tian, H. Du, Y. Zhang, and Z. Qu, Field-induced tricritical behavior in the Néel-type skyrmion host GaV_4S_8, Phys. Rev. B **102**, 094431 (2020).